Laser-Based Active Debris Removal: A Satellite Constellation Approach for Mitigating Small-Sized Space Debris in Low Earth Orbit

Original

Laser-Based Active Debris Removal: A Satellite Constellation Approach for Mitigating Small-Sized Space Debris in Low Earth Orbit / Lopez, Francesco; Mauro, Anna; Sfasciamuro, Domenico Edoardo; Semenzin, Silvia; Petronella, Nicolo; Bariselli, Federico; Helber, Bernd; Mauro, Stefano. - ELETTRONICO. - (2025), pp. 371-384. (23rd IAA Symposium on Space Debris Sydney (Aus) 29 September - 03 October 2025) [10.52202/083079-0037].

Publisher:
International Astronautical Federation (IAF)

Published
DOI:10.52202/083079-0037

76^{th} International Astronautical Congress (IAC) 2025 - Sydney, Australia

IAC-25,A6,5,6,x97884

Laser-Based Active Debris Removal: A Satellite Constellation Approach for Mitigating Small-Sized Space Debris in Low Earth Orbit

Francesco Lopez[1,2,*], Anna Mauro[1,3], Domenico Edoardo Sfasciamuro[1,4], Silvia Semenzin[4], Nicolò Petronella[4], Federico Bariselli[5], Bernd Helber[5], and Stefano Mauro[1,4]

[1] *ORIS, Turin, Italy*

[2] *Department of Energy, Politecnico di Torino, 10129, Torino, Italy*

[3] *Department of Electronics and Telecommunication, Politecnico di Torino, 10129, Torino, Italy*

[4] *Department of Mechanical & Aerospace Engineering, Politecnico di Torino, 10129, Torino, Italy*

[5] *Aeronautics and Aerospace Department, von Karman Institute for Fluid Dynamics, 1640, Sint-Genesius-Rode, Belgium*

[*]Corresponding author
Email: francesco.lopez@polito.it

Abstract

The growing issue of space debris poses a critical challenge as Earth's orbits become increasingly congested due to expanding space activities. Low Earth Orbit (LEO) is particularly affected, with an estimated 900 000 debris fragments ranging from 1 to 10 cm in size. These objects are large enough to penetrate spacecraft shielding yet too small to be effectively tracked, creating a severe and unpredictable collision risk. Existing mitigation strategies, such as end-of-life de-orbiting and graveyard orbit transfers, have proven insufficient in preventing debris accumulation. Consequently, Active Debris Removal (ADR) has emerged as a key research focus. Among proposed ADR techniques, laser ablation presents a promising solution, enabling remote, contactless trajectory alteration. This research investigates the feasibility of a laser-based ADR mission utilizing a constellation of satellites dedicated to debris detection and removal. Each satellite is designed with an advanced payload capable of autonomously identifying debris, assessing its trajectory, and engaging targets using a high-power pulsed laser system. The laser operates in the nanosecond pulse regime, with beam propagation characteristics analyzed for an effective operational range of approximately 100 km. A detailed study of laser-material interactions is conducted using a surface energy balance approach, complemented by a 3D heat conduction model that simulates the thermal response of debris under realistic conditions. This allows for the evaluation of the ablation area, the forces exerted on the debris surface, and the efficiency of the laser-induced momentum transfer. Based on the outcomes of this study, a dedicated satellite constellation is proposed, operating within an altitude range of 250 to 1 000 km and an inclination range of 60 to 105 degrees. The final architecture consists of approximately 20 satellites strategically positioned to maximize debris removal efficiency. Simulation results indicate that this system could successfully remove around 25% of small-sized debris within a 25-year timeframe, aligning with the guidelines set by the Inter-Agency Space Debris Coordination Committee (IADC).

1. Introduction

The accumulation of space debris in Earth orbit has become a critical challenge for the safety and sustainability of space operations. Since the dawn of the space age, the number of debris objects has consistently exceeded that of active satellites. This growing population poses a severe collision risk, particularly in LEO, where the density of operational assets is highest. The risk is amplified by the Kessler Syndrome [1], in which collisions between objects generate more debris, increasing the probability of further impacts in a self-sustaining chain reaction. While catastrophic events such as the Iridium–Cosmos collision [2] have significantly increased debris levels, the main contributors to the long-term growth of space debris are large, inactive objects left in orbit. Over time, these derelict satellites and upper stages degrade due to environmental factors, such as thermal cycling and radiation. Residual fuel or pressurants can lead to overpressure and explosions, further fragmenting these objects [3]. The resulting fragments, influenced by nodal precession, tend to spread into dense debris shells around Earth [4]. To address this, the IADC introduced mitigation guidelines in 2002, identifying two Protected Regions [5]: Region A (LEO), extending up to 2 000 km altitude, where post-mission disposal must ensure atmospheric reentry within 25 years; and Region B (GEO), spanning 35 586–35 986 km, where spacecraft are to be transferred to graveyard orbits. ESA's MASTER model [6] estimates the orbital debris population at over 34 000 objects larger than 10 cm, 900 000 between 1 and 10 cm, and more than 128 million fragments between 0.1 and 1 cm. The most hazardous altitudes lie between 700 and 1 000 km, particularly at inclinations from 60° to 105°. Among these, debris in the 1–10 cm range presents a critical challenge: too small for consistent tracking by current radar or optical systems, yet large enough to disable or destroy spacecraft. Effective mitigation of this population is essential to preserve the long-term viability of space activities.

To mitigate the growing risk posed by space debris, particularly in LEO, various regulations and passive de-orbiting strategies have been introduced. These include designing satellites to autonomously reenter Earth's atmosphere within 25 years of mission completion, as per international guidelines. While such passive measures have reduced the addition of new debris, they do not address the existing population of hazardous objects in orbit. This limitation has led to the development of ADR technologies, which are essential for long-term orbital sustainability. Among the proposed methods are robotic arms, nets, and harpoons, and support satellites [7]. Each offers specific advantages depending on the debris type, but they often share key limitations: they typically target large objects, involve direct contact, require complex rendezvous operations, and usually result in the destruction of the chaser satellite after a single use. In contrast, laser ablation presents a promising non-contact solution, particularly well-suited for small debris (1–10 cm) that is too small to track yet large enough to endanger operational spacecraft.

First proposed in the early 1990s [8], this technique involves directing high-energy laser pulses at debris to vaporize material on its surface, producing a plasma jet. This reaction imparts a recoil force that alters the debris's orbit, eventually causing it to reenter Earth's atmosphere due to enhanced atmospheric drag. Laser-based systems can be deployed from either ground-based or space-based platforms, with the latter offering major advantages: no atmospheric interference, shorter distances to targets, and better control over impulse direction [9]. Importantly, the required energy is far less than that needed for full vaporization, since only a small reduction in orbital velocity is needed to trigger reentry via a Hohmann-like transfer [10], as illustrated in Fig. 1.

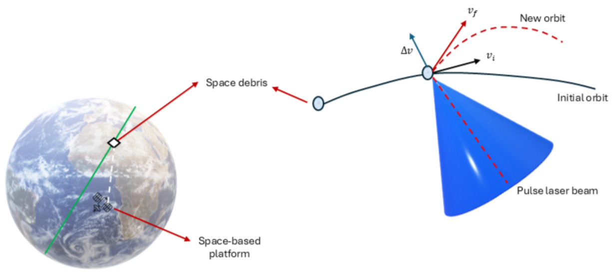

Figure 1: *Laser debris removal basic working principle.*

However, this technique is not without challenges. Delivering sufficient peak power in orbit places considerable demands on the satellite's electrical power system. Moreover, accurately predicting the resulting trajectory change is difficult, especially for irregularly shaped objects. As Sharring et al. [11] show, slight variations in orientation or geometry can lead to significant divergence in post-ablation trajectories. Nonetheless, targets with cooperative geometries, such as spheres, demonstrate predictable responses, reinforcing the method's viability for selected debris types. Given these advantages, laser ablation emerges as one of the most scalable and promising technologies for reducing the critical population of small, untrackable debris in LEO. It is therefore the primary focus of this study.

This study addressed key aspects of laser ablation for active debris removal in LEO. A nanosecond-pulsed laser was selected as the optimal compromise between energy efficiency and system feasibility. Laser-material interaction was analyzed through a 0D surface energy balance model and validated using a 3D thermal response simulation. The impact of plasma shielding and debris geometry was investigated, confirming that sufficient momentum transfer (ΔV of 50–100 m/s) can be achieved with short-duration laser activation. Different mission architectures are analyzed to identify the most suitable configuration for the case study. The region of interest spans 350–1 000 km altitude and 60°–105° inclination, defining the reference parameters. A study of debris populations in the 340–1 000 km range and their inclination distribution enables estimation of the time required for a single satellite to de-orbit all targets and the corresponding satellite count for each architecture.

2. Background Theory

Laser ablation is the process of removing material from a surface using high-energy laser pulses. Depending on pulse duration, removal occurs via thermal mechanisms (melting, vaporization, boiling) or non-thermal processes (e.g., electrostatic disruption). The interaction produces vapor, plasma, and particulates, and requires precise energy delivery, efficiently achieved with pulsed lasers. Compared to continuous-wave (CW) sources, pulsed lasers provide higher peak power and reduced thermal load, improving control and energy efficiency for momentum transfer applications such as debris removal [12].

The process develops in three stages [13]: (1) *bond breaking and plasma formation*, where absorbed energy initiates material removal; (2) *plasma expansion and cooling*, involving shock waves, non-equilibrium thermodynamics, and laser–plasma interactions (diffraction, shielding) that affect coupling; (3) *ejection and recondensation*, where vaporized material cools and condenses into particulates. These stages span femtoseconds (10^{-15} s) for absorption to milliseconds (10^{-3} s) for recondensation.

Pulse duration critically determines ablation dynamics. Nanosecond pulses drive thermal ablation with phase transitions and plasma shielding, while femtosecond pulses favor non-thermal processes such as Coulomb explosion, reducing diffusion and collateral damage. Thus, pulse width controls plume expansion, momentum coupling, and thermal effects.

Irimiciuc et al. [14] studied metals ablated with nanosecond (ns), picosecond (ps), and femtosecond (fs) pulses. All regimes exhibited plume splitting into fast (electrically driven) and slow (thermally driven) components. Nanosecond pulses produced broad, luminous plumes with higher velocities, while ps/fs pulses generated narrower, collimated plumes along the normal axis. For ultrashort pulses, plume velocity showed an inverse trend with heat of vaporization, confirming non-thermal dominance. fs-LIBS plumes also displayed narrower angular spreads and directional emission, improving control of momentum transfer and limiting secondary debris [15].

The momentum coupling coefficient quantifies momentum transfer efficiency:

$$c_{\mathrm{m}} = \frac{\Delta p}{E_{\mathrm{L}}}, \tag{1}$$

where Δp is imparted momentum and E_{L} the laser energy. Sharring et al. [11] identified three fluence regimes: (i) sub-threshold (no ablation), (ii) vaporization (rapid c_{m} increase), and (iii) plasma (shielding reduces c_{m}). Shorter pulses lower ablation thresholds and reach peak c_{m} at lower fluences, enhancing efficiency. Beam incidence also affects local fluence, $\Phi_{\mathrm{T}} = \Phi_{\mathrm{L}} \cos\theta$, introducing losses on irregular surfaces.

Sharring et al. [16] further distinguished two micropropulsion regimes. Short pulses ($\tau > 100$ ps) provide higher specific impulse (I_{sp}) due to faster ablation jets, while ultrashort pulses ($\tau < 100$ ps) offer smoother surface removal and lower thrust noise. Mass removal differs: short pulses promote vaporization, ultrashort pulses spallation or phase explosion. Although c_m values are comparable, I_sp for short pulses is about an order of magnitude higher. However, ultrashort pulses may allow higher optimal fluences Φ_opt, enhancing momentum coupling under specific conditions.

In summary, short pulses appear more effective for momentum-focused debris removal, whereas ultrashort pulses may offer benefits in precision and reduced noise.

For high-power debris removal, two laser architectures are viable: bulk solid-state lasers (e.g., Nd:YAG), with proven space heritage but thermal lensing issues, and fiber lasers, which offer up to 45% efficiency, excellent beam quality, and modular scalability [17, 18, 19]. Both can generate nanosecond pulses via Q-switching in the near-infrared. While bulk systems dominate current missions, fiber and diode-pumped architectures are increasingly preferred for their size, weight, power (SWaP) advantages and reduced complexity.

The most common wavelengths for space-based ablation are 1064 nm and its frequency-doubled 532 nm [20, 21, 22, 23]. In this study, $\lambda = 1064$ nm was selected for its proven ablation efficiency, strong flight heritage, and compatibility with both solid-state and fiber systems. Operating at 1064 nm also avoids the inefficiencies of frequency conversion, making the system more compact and robust.

Nanosecond pulses were chosen for their well-characterized thermal mechanisms and broad research basis, simplifying laser–matter interaction modeling. Prior micropropulsion studies [16] confirmed that ns pulses achieve optimal I_sp performance, reinforcing their suitability for thrust-oriented applications. In this work, pulses of 100 ns duration and 100 kHz repetition rate were selected. This corresponds to a duty cycle of $D = 1\%$, consistent with high-power laser requirements for efficient cooling and high pulse energy [24].

Beam propagation is modeled with a Gaussian profile to minimize divergence losses. A mobile optical system (mirrors and lenses) places the beam waist at the debris, neglecting defocusing or self-focusing effects, though these may become relevant in extreme regimes [25]. This configuration maximizes energy delivery to the target.

For the orbital dynamics studies of this work, the Gauss planetary equations are employed to model perturbations on debris orbits [26]. They link perturbative accelerations in radial, tangential, and normal directions to orbital element variations. For nearly circular orbits ($e \approx 0$), only the tangential component f_T affects the semi-major axis:

$$\frac{da}{dt} = 2 f_\mathrm{T} \frac{a^2}{\mu} V. \tag{2}$$

Atmospheric drag contributes:

$$\mathbf{f}_{\mathrm{T},1} = -\frac{1}{2}\rho C_\mathrm{d} \frac{A}{m} V_\mathrm{R}^2 \frac{\mathbf{V}_\mathrm{R}}{|\mathbf{V}_\mathrm{R}|} \cdot \frac{\mathbf{V}}{|\mathbf{V}|}, \tag{3}$$

where $\mathbf{V}_\mathrm{R} = \mathbf{V} - \boldsymbol{\omega} \times \mathbf{R}$ is the relative velocity to the rotating atmosphere.

Solar radiation pressure adds:

$$\mathbf{f}_{\mathrm{T},2} = -P_\mathrm{s} K \frac{A}{m} \frac{\mathbf{R}_\mathrm{S}}{|\mathbf{R}_\mathrm{S}|} \cdot \frac{\mathbf{V}}{|\mathbf{V}|}, \tag{4}$$

with $\mathbf{R}_\mathrm{S} = \mathbf{R}_\text{e-s} + \mathbf{R}$.

The combined perturbation is:

$$\frac{da}{dt} = 2(f_{\mathrm{T},1} + f_{\mathrm{T},2}) \frac{a^2}{\mu} V. \tag{5}$$

Laser ablation adds thrust through material ejection [27]:

$$F_\mathrm{thrust} = \phi_\mathrm{eff} A_{target} C_\mathrm{m} f, \tag{6}$$

where $\phi_\mathrm{eff} = T_\mathrm{eff}\phi$ accounts for system losses, A_target is the illuminated area, C_m the thrust coefficient, and f the repetition frequency. Laser fluence is:

$$\phi = \frac{E_\mathrm{pulse}}{\frac{1}{2}\pi\omega(L)^2}, \tag{7}$$

with E_pulse the pulse energy and $\omega(L)$ the beam radius at $1/e^2$ intensity.

This thrust produces a ΔV opposing the orbital velocity, reducing the semi-major axis. For initial velocity:

$$v_\mathrm{i} = \sqrt{\frac{\mu}{R_\mathrm{earth} + h_\mathrm{sat}}}, \quad v_\mathrm{f} = v_\mathrm{i} - \Delta V, \tag{8}$$

the final orbital energy and semi-major axis are:

$$\epsilon_\mathrm{f} = \frac{v_\mathrm{f}^2}{2} - \frac{\mu}{r_\mathrm{f}} = -\frac{\mu}{2a_\mathrm{f}}, \quad a_\mathrm{f} = -\frac{\mu}{2\epsilon_\mathrm{f}}, \tag{9}$$

$$da = a_\mathrm{f} - a_\mathrm{i}. \tag{10}$$

This framework enables quantification of laser-induced semi-major axis reduction under realistic orbital conditions.

3. High-power laser payload design

Model overview. A synthetic, steady-state 0D model is developed to evaluate the temperature evolution and ablation dynamics of space-debris surfaces under laser irradiation. The model employs surface energy-balance principles, incorporating laser heating as the primary source while accounting for losses via vaporization latent heat and radiative dissipation to space. Thermal conduction effects are excluded from the current formulation, and material thermal properties are assumed temperature-independent for computational efficiency.

Laser–plasma interaction and parameter search. The model incorporates laser–plasma interaction effects, particularly plasma shielding phenomena that attenuate laser intensity at the target surface [28, 13, 29], providing more realistic energy-deposition estimates. Comprehensive simulations are used to identify optimal laser parameters (pulse duration, repetition rate, and power density). Additionally, preliminary force estimates on debris surfaces and required laser firing durations are obtained.

Materials and properties. Although four materials were considered in the property database, detailed results are presented here for aluminum as a representative case, given its prevalence in orbital debris. The selected material properties used in this study are reported in Tab. 1.

Table 1: *Material properties for aluminum, copper, titanium, and silica.*

Property	**Aluminum**	**Copper**	**Titanium**	**Silica**
L_vap [J/kg]	$10.5 \cdot 10^6$	$4.73 \cdot 10^6$	$9 \cdot 10^6$	$10 \cdot 10^6$
k_cond [W/mK]	237	380	21.9	2
ρ [kg/m^3]	2700	8930	4500	2242.6
T_melt [K]	933	1358	1941	1983
T_vap [K]	2793	2836	3560	3000
R [kg]	0.3	0.3	0.3	0.3

Power balance. To estimate the necessary laser peak power, a target temperature sufficient for material vaporization is imposed. In a steady-state regime, with constant temperature over time, the system is governed by the following power-balance equation:

$$\dot{Q}_\mathrm{laser} = \dot{Q}_\mathrm{loss} = \epsilon\sigma\left(T_\mathrm{w}^4 - T_\mathrm{env}^4\right) + \phi_\mathrm{vap}L_\mathrm{vap} + k_\mathrm{cond}\frac{T_\mathrm{w} - T_\mathrm{env}}{L_c} \tag{11}$$

where the irradiation term is modeled with the Stefan–Boltzmann law for radiative heat transfer between the object and deep space, the vaporization term is modeled considering the Langmuir formula where L_vap is the latent heat of vaporization of the debris material and ϕ_vap is the evaporation mass flux computed through the Knudsen–Langmuir formula, and the last term represents heat-conduction loss.

The source term is modeled as follows:

$$\dot{Q}_\mathrm{laser} = (1 - R)I_\mathrm{avg}e^{-\tau}, \tag{12}$$

where I_avg is the laser irradiance averaged over one period. The exponential term accounts for plasma shielding. Quantity R represents the material reflectivity, where $\epsilon = 1 - R$. The incident intensity I splits into an absorbed fraction $I_\mathrm{abs} = \epsilon I$ and a reflected fraction $I_\mathrm{refl} = RI$ [30].

Neutral plume model. For the plume, a model for neutral-plume expansion in free-molecular flow is implemented. The plume number density n is obtained from a code developed at VKI [31], which implements the method proposed by Cai and Boyd [32]. The number density decreases with distance from the target surface. To estimate the number density at each axial distance x, the mean value is computed by averaging over the laser-beam cross-section.

Ionization and absorption. The degree of ionization in the plasma is derived from the Saha–Eggert equation [33]:

$$\frac{\eta_e \eta_{i1}}{\eta_0} = \frac{\left(\frac{2\pi m_e k_B T}{h^2}\right)^{\frac{3}{2}} \exp\left(-\frac{I_P}{k_B T}\right)}{n}, \tag{13}$$

where η_e, η_{i1}, and η_0 are the molar fractions of electrons, singly charged aluminum ions, and neutral atoms, respectively (Eq. 14) [34]. Second- and higher-order ionization is neglected. Additionally, m_e is the electron mass, h is Planck's constant, and n is the number density.

$$\eta_j = \frac{n_j}{n} \quad \text{with} \quad j = \text{e}, \text{i}, 0. \tag{14}$$

Additionally, by considering particles' conservation:

$$n = \sum n_j = n_0 + n_{i1} + n_e, \tag{15}$$

$$\eta_0 + \eta_{i1} + \eta_e = 1. \tag{16}$$

and considering a neutral plasma:

$$\eta_{i1} = \eta_e. \tag{17}$$

Thus, Eq. 13 can be solved for η_e and η_0 to obtain the degree of ionization in the plume, under the assumption of thermodynamic equilibrium.

Once the ionization fractions are known, the plasma absorption coefficient can be calculated. During ablation, plasma absorbs part of the laser energy (plasma shielding). The IB absorption coefficient, α_{IB}, has two contributions: ion ($\alpha_{IB,e\text{-}i}$) and neutral ($\alpha_{IB,e\text{-}n}$) [34, 28, 29]:

$$\alpha_{IB,e\text{-}n} = \left[1 - \exp\left(-\frac{hc}{\lambda k_B T}\right)\right] Q n_e n_0 \tag{18}$$

$$\alpha_{IB,e\text{-}i} = \left[1 - \exp\left(-\frac{hc}{\lambda k_B T}\right)\right] \frac{4e^6 \lambda^3 n_e}{3hc^4 m_e} \times \left(\frac{2\pi}{3 m_e k_B T}\right)^{1/2} n_i \tag{19}$$

where n_i is the ion number density and e is the elementary charge in statcoulombs.

The absorption coefficient thus contributes to the required laser peak power, because the on-surface power is reduced by surface reflectivity and plasma optical thickness, as in Eq. 20:

$$I_{abs} = \epsilon I_0 e^{-\tau}, \tag{20}$$

with τ the plasma optical thickness, i.e., the portion of laser power absorbed by the plume via IB and not reaching the surface. It is calculated as

$$\tau = \int_0^L \alpha_{IB}(x)\, dx. \tag{21}$$

Irradiance sizing. The laser power can be designed for each material following this scheme:

- the required irradiance, averaged over one period:

$$I_{avg} = \frac{\dot{Q}_{loss}}{\epsilon e^{-\tau}}. \tag{22}$$

- the peak (in time) irradiance needed to maintain the vaporization temperature is obtained by inverting:

$$I_{avg} = \frac{I_{peak,t} \tau_{pulse}}{T}, \tag{23}$$

  where the period T is the inverse of the laser frequency. This $I_{peak,t}$ is assumed to be the mean irradiance of the Gaussian beam, such that $I_0 = 2I_{peak,t}$, while P_0 is then calculated from

$$I_0 = \frac{2P_0}{\pi w_0^2}. \tag{24}$$

Maps and results. The ionization degree as a function of the distance x from the target surface for four plume temperatures is reported in Fig. 2.

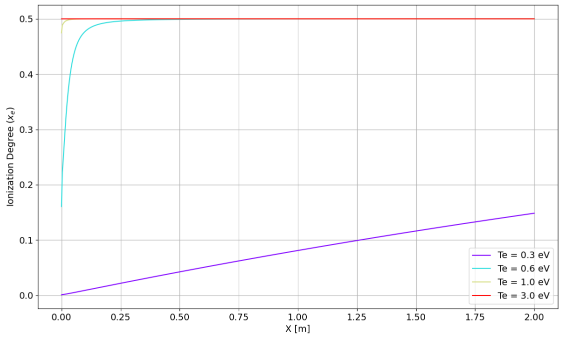

Figure 2: *Ionization degree for varying distance from the target surface, for different plume temperatures.*

The α_{IB} trend for increasing plume temperature is reported in Fig. 3. Here, the reference value for the plume number density is taken as the equilibrium number density at the surface.

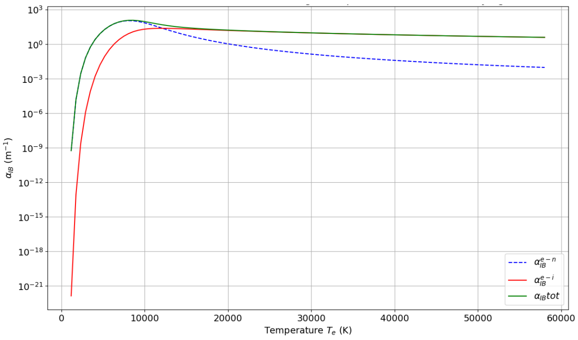

Figure 3: *Aluminum α_{IB} values for varying T_e.*

A calculation of α_{IB} is conducted by solving the Saha equation for different plume temperatures while incorporating the exact vapor number-density distribution within the plume. Representative T_{e} values are 0.3, 0.6, 1, and 3 eV (approximately 3 480, 6 960, 11 600, and 34 800 K). The plume temperature is imposed; a detailed study of temperature determination from laser–plume coupling is not pursued here. The ionization degree is computed for each fixed T_{e}, allowing the calculation of $\alpha_{\text{IB,e-n}}$ and $\alpha_{\text{IB,e-i}}$. The variation of α_{IB} with axial distance is shown in Fig. 4 for each T_{e}.

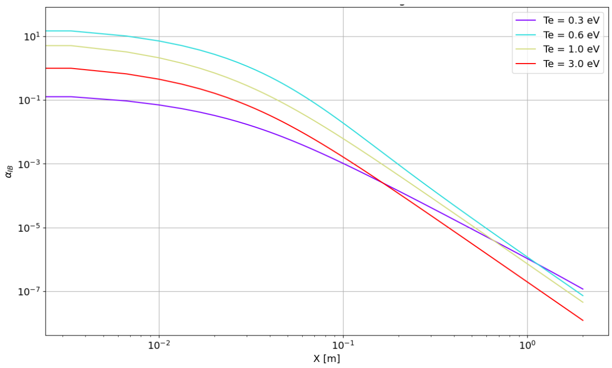

Figure 4: *α_{IB} as a function of the distance from an aluminum target surface.*

Aluminum case: absorption and power. In Tables 2 and 3, the results for aluminum are reported in terms of plasma absorption and the resulting required laser power. All results assume $r_{\text{abl}} = w_0$ (the entire area affected by the laser reaches the vaporization temperature) and two ablated areas: $r_{abl,1} = 2.5$ cm and $r_{abl,2} = 1.25$ cm.

Table 2: *Results for various electron temperatures T_e of aluminum with ablation radius $r_{abl} = 2.5$ cm.*

Aluminum, $r_{\text{abl}} = 2.5$ cm					
T_{e} **(eV)**	τ	$e^{-\tau}$	**Abs. Coeff.**	I_{avg} **(MW/m^2)**	**P$_0$ (MW)**
0.3	0.13541	0.8734	0.61135	961.63	188.82
0.6	0.08379	0.9196	0.64374	913.26	179.32
1.0	0.05217	0.9492	0.66442	884.83	173.74
3.0	0.01411	0.9860	0.69019	851.79	167.25

Table 3: *Results for various electron temperatures T_e of aluminum with ablation radius $r_{abl} = 1.25$ cm.*

Aluminum, $r_{\text{abl}} = 1.25$ cm					
T_{e} **(eV)**	τ	$e^{-\tau}$	**Abs. Coeff.**	I_{avg} **(MW/m^2)**	**P$_0$ (MW)**
0.3	0.05210	0.9492	0.66446	884.77	43.43
0.6	0.03224	0.9683	0.67779	867.37	42.58
1.0	0.02007	0.9801	0.68609	856.88	42.06
3.0	0.00543	0.9946	0.69621	844.42	41.45

Preliminary force and on-time. The forces obtained on the debris can be estimated assuming the worst-case absorption ($T_{\text{e}} = 0.3\,\text{eV}$) and a uniform temperature distribution equal to the vaporization temperature over the ablated surface. The ablated area is

$$A_{\text{abl}} = \pi r_{\text{abl}}^2. \tag{25}$$

The force acting on the debris is calculated using

$$F_{\text{debris}} = \phi_{\text{vap}} v_{\text{vap}} A_{\text{abl}}, \tag{26}$$

where ϕ_{vap} describes the number of particles escaping per unit area and time, v_{vap} is the vapor flow speed (average speed of the Maxwellian), and A_{abl} is the ablated area [29]. The corresponding on-time to achieve a target ΔV follows

$$F_{\text{debris}} = m_{\text{debris}} \frac{\Delta V}{\Delta t_{\text{on}}}. \tag{27}$$

Table 4: *Estimated force and activation times for different aluminum debris shapes and ablation radii.*

Shape	***F* (N)**	$\Delta V = 50\,\mathrm{m/s}$		$\Delta V = 100\,\mathrm{m/s}$	
		Δt_{on} **(s)**	**Ablated mass [%]**	Δt_{on} **(s)**	**Ablated mass [%]**
		Aluminum, $r_{\text{abl}} = 2.5\,\mathrm{cm}$			
Cube	81.00	0.2100	6.81	0.4000	12.97
Plate	81.00	0.1700	6.89	0.3200	12.97
Sphere	81.00	0.1100	6.81	0.2100	13.01
		Aluminum, $r_{\text{abl}} = 1.25\,\mathrm{cm}$			
Cube	20.25	0.8100	6.57	1.5600	12.65
Plate	20.25	0.6500	6.59	1.2500	12.67
Sphere	20.25	0.4300	6.66	0.8200	12.70

Results for aluminum are reported in Tab. 4. A more precise calculation will be reported in Section 4 based on 3D simulations, which resolve the surface-temperature distribution and thus the force.

4. 3D time-dependent simulations of space debris thermal response

A 3D time-dependent model is implemented in COMSOL Multiphysics to simulate heat distribution on the debris surface as it reaches the ablation threshold. The inputs for this model are the laser parameters obtained from the analysis in Section 3. Thanks to this model, a more precise temperature distribution is obtained. From this, the forces on the debris can be calculated. Aluminum is chosen as the test material for these simulations and the debris is approximated with different shapes: a cube, a flat plate, and a sphere.

Boundary conditions for radiation towards space, vaporization, and the incoming laser beam are implemented. The loss due to vaporization is accounted for by introducing an outward heat flux. The heat flux calculation is based on the formula in Eq. 28 while the laser is modeled with a Gaussian beam propagation:

$$\dot{Q}_{\text{vap}} = \phi_{\text{vap}} L_{\text{vap}}. \tag{28}$$

$$\phi_{\text{vap}} = n_{\text{w}}^{\text{eq}} \sqrt{\frac{\mu k_{\text{B}} T_{\text{w}}}{2\pi}}. \tag{29}$$

The chosen heat transfer interface is the *Heat Transfer in Solids* module, which is used to model heat transfer by conduction, convection, and radiation. By default, a solid model is active on all domains, and functionality for including other domain types, such as fluid domains, is also available. For the cube, the temperature evolutions in point A (maximum temperature on the surface) and B ($r = r_{\text{abl}} = 1.25$ cm) until $t = 0.5$ s are reported in Fig. 5. In Fig. 6, the visual representation of the cube temperature distribution is shown, with the heated zones displayed on the cube using color gradients. The visual representation of the temperature distribution is also reported for the plate and sphere debris, respectively, in Figs. 7 and 8.

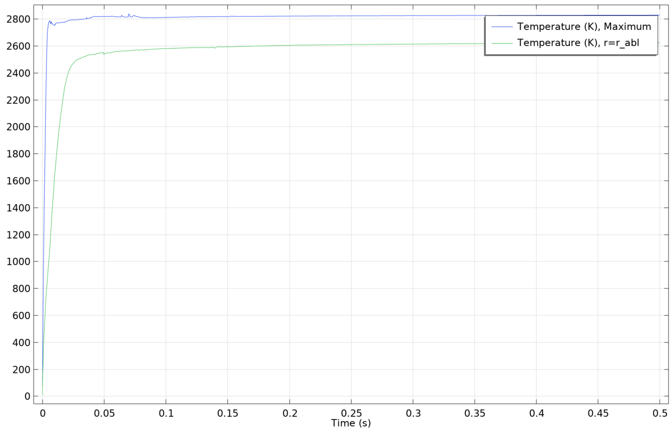

Figure 5: *Temperatures in the aluminum cube.*

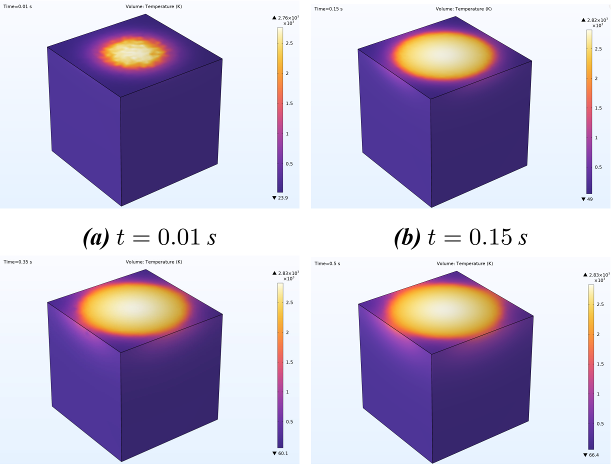

(a) $t = 0.01\ s$

(b) $t = 0.15\ s$

(c) $t = 0.35\ s$

(d) $t = 0.50\ s$

Figure 6: *Temperature distribution on the aluminum cube at different time instants.*

It is possible to obtain the effective forces exerted on the debris thanks to the precise surface temper-

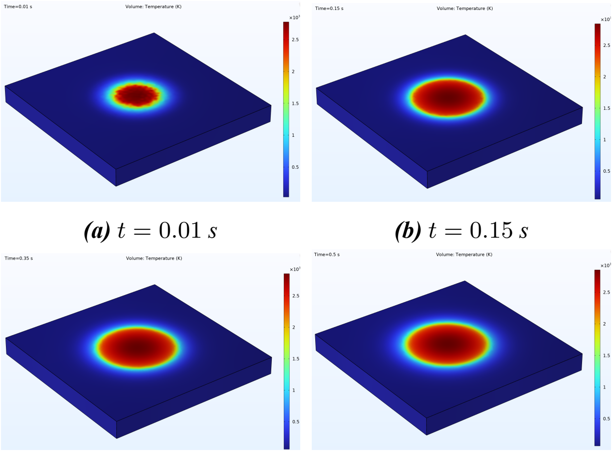

(a) $t = 0.01\,s$ ***(b)*** $t = 0.15\,s$

(c) $t = 0.35\,s$ ***(d)*** $t = 0.50\,s$

Figure 7: *Temperature distribution on the aluminum flat plate.*

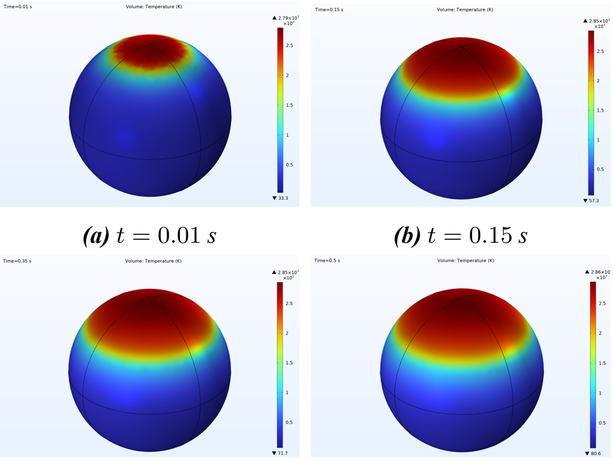

(a) $t = 0.01\,s$ ***(b)*** $t = 0.15\,s$

(c) $t = 0.35\,s$ ***(d)*** $t = 0.50\,s$

Figure 8: *Temperatures in the aluminum sphere.*

ature distribution. As the temperature continues to rise over time, including in areas outside the direct laser beam, the force is computed as a function of time through the following procedure: VTK files containing unstructured grid information and associated temperature data are exported from COMSOL at each time step, subsequently processed in Python to calculate mean temperature values for each computational cell, and finally used to determine the infinitesimal force contribution from each cell, considering its vector components in the x, y, and z directions. In Fig. 9, the evolution over time of the three force components is shown for the sphere debris. A representation of the forces inclined with respect to the beam direction is shown in Fig. 10.

By considering the variation of the force over time, it is possible to calculate the ΔV achieved on the debris surface by integrating the force over time:

$$\Delta V = \int_{t_0}^{t_f} \frac{F(t)}{m(t)}\,dt \tag{30}$$

The evolution in time of the ΔV for the aluminum sphere is reported in Fig. 11.

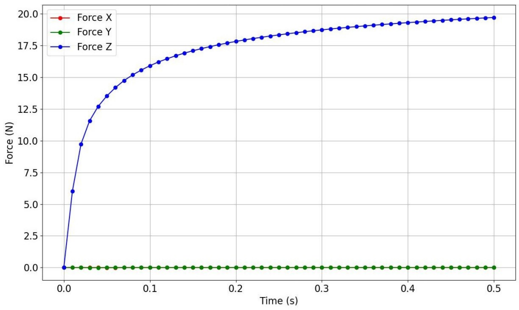

Figure 9: *Evolution of force components over time for the aluminum sphere.*

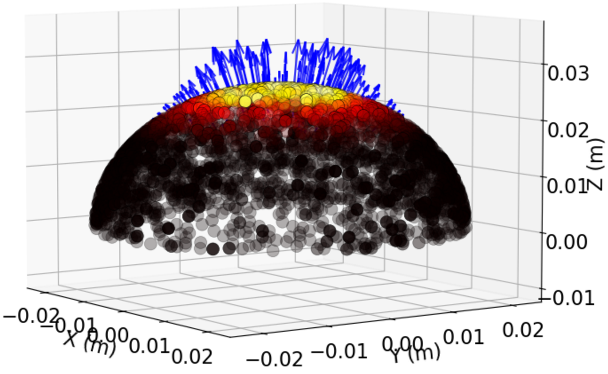

Figure 10: *Vector representation of particle emission from the surface of the sphere.*

5. Orbital Analysis

To estimate mission duration and the required number of satellites, the debris population is characterized across altitude and inclination ranges. In the protected LEO region, approximately 9×10^5 objects of 1–10 cm exist [35]. Direct simulation of satellite–debris interactions are computationally in-

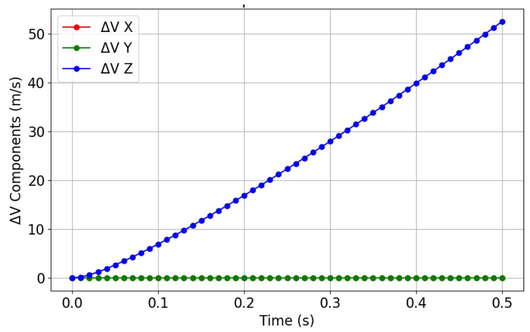

***Figure 11:** Evolution of ΔV components over time for the aluminum sphere.*

feasible; therefore, a geometric probability approach is adopted.

For altitudes $h = 350$–$1\,000$ km, the debris distribution is derived from a triple integral, yielding $\sim 2.1 \times 10^5$ objects (about 23% of the total). The operational visibility range is set to $\Delta h = \pm 19$ km. For instance, at $h = 981$ km the relevant interval is [962, 1 000] km.

Inclination analysis shows that most debris lies within $i = 60°$–$105°$, divided into three sub-ranges:

- $\Delta i_1 = 60°$–$75°$ (15%),
- $\Delta i_2 = 75°$–$90°$ (25%),
- $\Delta i_3 = 90°$–$105°$ (40%).

The remaining 20% is located below $i = 60°$.

To ensure coverage, the orbital spacing is set to $\Delta i = \pm 7.5°$ and $\Delta\text{RAAN} = \pm 9°$. The full range $\Omega = [0°, 180°]$ is divided into 10 RAAN intervals. Each interval hosts three orbital planes, one per inclination band, giving a total of 30 planes.

Geometric probability framework. Debris density is evaluated over a spherical shell between radii r_1 and r_2, with mean radius:

$$r_{\text{sat}} = \frac{r_1 + r_2}{2}. \tag{31}$$

The volume of this spherical shell is:

$$V_{\text{bond}} = \int_0^{2\pi} \int_{\text{lat}_{\min}}^{\text{lat}_{\max}} \int_{r_1}^{r_2} r^2 \sin\phi \, dr \, d\phi \, d\theta, \tag{32}$$

where the latitude bounds depend on the inclination.

The satellite's visibility cone, of radius Δh, sweeps a toroidal volume during one orbit:

$$V_{\text{tor}} = 2\pi^2 r_{\text{sat}} \Delta h^2. \tag{33}$$

Debris density within the n-th range is:

$$\rho_n = \frac{N_{\text{deb},n}}{V_{\text{bond},n}}. \tag{34}$$

where $N_{\text{deb},n}$ is the total number of debris estimated in the n-th range. The expected number of debris encountered per orbit, within the n-th range, is:

$$N_{\text{deb/o},n} = \frac{V_{\text{tor},n}}{N_{\text{orbit}}} \rho_n. \tag{35}$$

The required number of orbits to engage all debris, within the n-th range, is:

$$N_{\text{TotalOrbits,n}} = \frac{N_{\text{deb},n}}{N_{\text{deb/o},n}}. \tag{36}$$

Hence, the mission time, for the n-th range, is obtained as:

$$t_{\text{tot},n} = N_{\text{TotalOrbits,n}} T_{\text{orbit},n}, \tag{37}$$

with orbital period

$$T_{\text{orbit},n} = 2\pi \sqrt{\frac{r_{\text{sat},n}^3}{\mu}}. \tag{38}$$

Mission duration estimates. For the altitude interval [350, 1000] km, estimated durations are:

- Inclination range 60°–75°: 20 years,
- Inclination range 75°–90°: 21 years,
- Inclination range 90°–105°: 27 years.

Constellation architecture. The proposed architecture employs LiDAR-based debris identification, enabling detection and tracking within ±19 km of the satellite altitude. A total of 40 satellites is foreseen. The required ΔV for changing the semi-major axis is computed with a Hohmann transfer:

$$\Delta V_{\text{TOT}} = \Delta V_1 + \Delta V_2, \tag{39}$$

with

$$\Delta V_1 = \sqrt{\frac{\mu}{r_1}} \left(\sqrt{\frac{2 r_2}{r_1 + r_2}} - 1 \right), \tag{40}$$

$$\Delta V_2 = \sqrt{\frac{\mu}{r_2}}\left(1 - \sqrt{\frac{2r_1}{r_1 + r_2}}\right). \quad (41)$$

The Hohmann transfer time is:

$$t_{\mathrm{H}} = \frac{\pi\sqrt{a^3}}{\sqrt{\mu}}. \quad (42)$$

This configuration balances performance, cost, and flexibility, and provides nearly equal operational times across inclination ranges:

- 60°–75°: 20 years,
- 75°–90°: 21 years,
- 90°–105°: 27 years.

Sensitivity to object properties. Results are presented for debris with different geometries: thin aluminium plates and aluminium spheres. Plates are analyzed for multiple drag coefficients ($C_{\mathrm{d}} = 0.47, 0.92, 2.0$). Two spherical reference cases are considered ($R_1 = 0.5$ cm, $R_2 = 1.5$ cm).

Tables 5, 6, and 7 show that de-orbiting times vary significantly with object properties. For the highest altitude bin [962–1000] km, natural decay exceeds 800 years. Increasing C_{d} reduces this to 308 years, while applying $\Delta V = 100$ m/s lowers the time further to only 25.6 years, demonstrating the effectiveness of the proposed approach.

Table 5: *De-orbiting time (years) – Thin plate* 5×5 cm^2, $C_d = 0.47$, *aluminium*

Altitude range [km]	$T_{\mathrm{do}\,\vert\,\Delta V=0\,\mathrm{m/s}}$	$T_{\mathrm{do}\,\vert\,\Delta V=50\,\mathrm{m/s}}$	$T_{\mathrm{do}\,\vert\,\Delta V=100\,\mathrm{m/s}}$
354–392	0.5–0.8		
392–430	0.8–1.2		
430–468	1.2–1.9		
468–506	3.0–4.8		
506–544	4.8–7.5	1.1–1.6	
544–582	7.5–11.8	1.6–2.6	
582–620	11.8–19.1	2.6–4.0	
620–658	19.1–29.3	4.0–6.2	1.4–2.2
658–696	29.3–50.0	6.2–9.4	2.2–3.4
696–734	50.0–76.6	9.4–15.1	3.4–5.4
734–772	76.6–124.3	15.1–21.8	5.4–8.2
772–810	124.3–142.7	21.8–43.3	8.2–12.6
810–848	142.7–298.6	43.3–56.0	12.6–20.0
848–886	298.6–532.0	56.0–90.7	20.0–29.1
886–924	532.0–800+	90.7–129.4	29.1–42.7
924–962	800+	129.4–287.2	42.7–67.1
962–1000	800+	287.2–685.7	67.1–132.8

Table 6: *De-orbiting time (years) – Thin plate* 5×5 cm^2, $C_d = 0.92$, *aluminium*

Altitude range [km]	$T_{\mathrm{do}\,\vert\,\Delta V=0\,\mathrm{m/s}}$	$T_{\mathrm{do}\,\vert\,\Delta V=50\,\mathrm{m/s}}$	$T_{\mathrm{do}\,\vert\,\Delta V=100\,\mathrm{m/s}}$
354–392	0.3–0.4		
392–430	0.4–0.7		
430–468	0.7–1.0		
468–506	1.0–1.6		
506–544	1.6–2.5		
544–582	2.5–3.9		
582–620	3.9–6.2	1.3–2.1	
620–658	6.2–9.4	2.1–3.3	
658–696	9.4–16.0	3.3–4.8	
696–734	16.0–25.4	4.8–8.0	1.9–2.7
734–772	25.4–34.2	8.0–12.7	2.7–4.0
772–810	34.2–54.6	12.7–17.4	4.0–6.7
810–848	54.6–94.9	17.4–30.2	6.7–10.1
848–886	94.9–165.3	30.2–40.1	10.1–14.6
886–924	165.3–228.5	40.1–77.8	14.6–25.5
924–962	228.5–491.6	77.8–136.9	25.5–41.8
962–1000	800+	136.9–183.0	41.8–63.7

Table 7: *De-orbiting time (years) – Thin plate* 5×5 cm^2, $C_d = 2.0$, *aluminium*

Altitude range [km]	$T_{\mathrm{do}\,\vert\,\Delta V=0\,\mathrm{m/s}}$	$T_{\mathrm{do}\,\vert\,\Delta V=50\,\mathrm{m/s}}$	$T_{\mathrm{do}\,\vert\,\Delta V=100\,\mathrm{m/s}}$
354–392	0.1–0.2		
392–430	0.2–0.3		
430–468	0.3–0.5		
468–506	0.5–0.8		
506–544	0.8–1.2		
544–582	1.2–1.8		
582–620	1.8–2.8		
620–658	2.8–4.7		
658–696	4.7–6.9	1.5–2.3	
696–734	6.9–10.9	2.3–3.6	
734–772	10.9–15.8	3.6–5.5	
772–810	15.8–27.2	5.5–9.2	
810–848	27.2–42.7	9.2–14.0	
848–886	42.7–69.5	14.0–21.2	
886–924	69.5–86.5	21.2–31.3	7.1–10.5
924–962	86.5–201.8	31.3–55.3	10.5–18.7
962–1000	201.8–308.2	55.3–81.2	18.7–25.6

Population-level estimate. Finally, a representative debris population is assumed with the following distribution:

- thin plate (5×5 cm), $C_{\mathrm{d}} = 0.92$: 25%;
- thin plate (10×10 cm), $C_{\mathrm{d}} = 0.92$: 10%;
- sphere ($R = 1.5$ cm), $C_{\mathrm{d}} = 2$: 60%;
- thin cylinder ($R = 0.5$ cm, $H = 2$ cm), $C_{\mathrm{d}} = 0.72$: 5%.

The weighted average leads to a minimum operational altitude of 563 km, higher than the previously assumed 373 km. Thus, the effective constellation operational range extends from 544 to 1 000 km. For this updated range, mission durations are:

- 60°–75°: 16 years,
- 75°–90°: 17 years,
- 90°–105°: 17 years.

The orbital analysis demonstrates that a purely geometric–probabilistic framework can yield consistent estimates of debris encounter rates, constellation sizing, and mission duration. The results confirm that the debris population is highly concentrated in the 60°–105° inclination band, requiring a multiplane architecture to ensure uniform coverage. Sensitivity studies highlight that object properties such as shape and drag coefficient significantly influence natural de-orbiting times, making active intervention essential, especially above 800 km where lifetimes can exceed centuries.

By integrating the debris population model, geometric visibility, and orbital mechanics, the proposed constellation of 40 satellites achieves a balanced trade-off between operational lifetime, altitude coverage, and cost. The analysis also underscores the effectiveness of modest orbital maneuvers, which reduce de-orbiting times by more than an order of magnitude.

6. Conclusion

This study demonstrated the feasibility of a space-based laser ablation constellation for active debris removal in LEO. Through combined modeling, 3D simulations, and orbital analysis, key design parameters were identified, confirming that a 20–40 satellite system could reduce the critical 1–10 cm debris population by approximately 25% within 25 years. While the concept shows strong potential, future work should focus on experimental validation and system integration to ensure readiness for operational deployment.

References

[1] D. J. Kessler, “The kessler syndrome,” 2009.

[2] N. L. Johnson, “The collision of iridium 33 and cosmos 2251: The shape of things to come,” in *60th International Astronautical Congress*, (Daejeon, Republic of Korea), NASA Johnson Space Center, October 2009.

[3] S. H. Choi, “Assessment study of small space debris removal by laser satellites,” 2011.

[4] L. Walker and M. Vasile, “Mitigation of debris in leo using space-based lasers,” in *72nd International Astronautical Congress (IAC)*, International Astronautical Federation (IAF), IAF, 2021.

[5] Inter-Agency Space Debris Coordination Committee (IADC), “IADC Space Debris Mitigation Guidelines,” Tech. Rep. IADC-02-01, Revision 1, September 2007. Issued by Steering Group and Working Group 4.

[6] ESA Space Debris Office, “ESA’s Annual Space Environment Report,” tech. rep., European Space Agency (ESA), ESA ESOC, Robert-Bosch-Strasse 5, D-64293 Darmstadt, Germany, July 2024. GEN-DB-LOG-00288-OPS-SD, Final Version.

[7] C. P. Mark and S. Kamath, “Review of active space debris removal methods,” *Space Policy*, vol. 47, pp. 194–206, 2019.

[8] W. O. Schall, “Orbital debris removal by laser radiation,” *Acta Astronautica*, vol. 24, pp. 343–351, 1991. International Astronautical Federation Congress.

[9] L. Walker and M. Vasile, “Mitigation of debris in LEO using Space-Based lasers,” in *72nd International Astronautical Congress (IAC)*, IAC-21-A6.4.4, (Dubai, United Arab Emirates), International Astronautical Federation, IAF, October 2021.

[10] D. Liedahl, A. Rubenchik, S. Libby, S. Nikolaev, and C. Phipps, “Pulsed laser interactions with space debris: Target shape effects,” *Advances in Space Research*, vol. 52, no. 5, pp. 895–915, 2013.

[11] S. Scharring, J. Wilken, and H.-A. Eckel,

"Laser-based removal of irregularly shaped space debris," *Optical Engineering*, vol. 56, no. 1, p. 011007, 2016.

[12] L. Hou, F. Yin, S. Wang, J. Sun, and H. Yin, "A review of thermal effects and substrate damage control in laser cleaning," *Optics & Laser Technology*, vol. 174, p. 110613, 2024.

[13] R. Russo, X. L. Ma, J. Yoo, and J. J. Gonzalez, *Laser-Induced Breakdown Spectroscopy, Chapter 3: Laser Ablation*. Elsevier Science, 2020.

[14] S. A. Irimiciuc, P.-E. Nica, M. Agop, and C. Focsa, "Target properties – plasma dynamics relationship in laser ablation of metals: Common trends for fs, ps and ns irradiation regimes," *Applied Surface Science*, vol. 506, p. 144926, 2020.

[15] S. Harilal, "Comparison of nanosecond and femtosecond libs," 06 2013.

[16] S. Scharring, R.-A. Lorbeer, and H.-A. Eckel, "Numerical simulations on laser-ablative micropropulsion with short and ultrashort laser pulses," *Transactions of the Japan Society for Aeronautical and Space Sciences*, vol. 14, 09 2016.

[17] A. Yu, S. Li, G. Shaw, A. Seas, M. Stephen, E. Troupaki, A. Vasilyev, L. Ramos-Izquierdo, A. Lukemier, W. Mamakos, A. Melak, and J. Guzek, "Overview of space qualified solid-state lasers development at nasa goddard space flight center," vol. 7193, 02 2009.

[18] M. Krainak, A. Yu, M. Stephen, S. Merritt, L. Glebov, L. Glebova, A. Ryasnyanskiy, V. Smirnov, X. Mu, S. Meissner, and H. Meissner, "Monolithic solid-state lasers for spaceflight," *Proceedings of SPIE - The International Society for Optical Engineering*, vol. 9342, 02 2015.

[19] A. W. Yu, M. A. Stephen, S. X. Li, G. B. Shaw, A. Seas, E. Dowdye, E. Troupaki, P. Liiva, D. Poulios, and K. Mascetti, "Space laser transmitter development for ICESat-2 mission," in *Solid State Lasers XIX: Technology and Devices* (W. A. Clarkson, N. Hodgson, and R. K. Shori, eds.), vol. 7578, p. 757809, International Society for Optics and Photonics, SPIE, 2010.

[20] D. E. Smith, M. T. Zuber, H. V. Frey, J. B. Garvin, J. W. Head, D. O. Muhleman, G. H. Pettengill, R. J. Phillips, S. C. Solomon, H. J. Zwally, W. B. Banerdt, T. C. Duxbury, M. P. Golombek, F. G. Lemoine, G. A. Neumann, D. D. Rowlands, O. Aharonson, P. G. Ford, A. B. Ivanov, C. L. Johnson, P. J. McGovern, J. B. Abshire, R. S. Afzal, and X. Sun, "Mars orbiter laser altimeter: Experiment summary after the first year of global mapping of mars," *Journal of Geophysical Research: Planets*, vol. 106, no. E10, pp. 23689–23722, 2001.

[21] O. Le Rille, A. Straume, M. Vieitez, W. Ubachs, W. Water, B. Witschas, O. Reitebuch, G. Marseille, J. Kloe, A. Stoffelen, H. K., H. Körnich, and H. Schyberg, "Esa´s wind lidar mission adm-aeolus: On-going scientific activities related to calibration, retrieval and instrument operation," 07 2010.

[22] D. Winker, C. Hostetler, and W. Hunt, "Caliop: the calipso lidar," vol. 561, p. 941, 05 2004.

[23] J. Abshire, E. Ketchum, R. Afzal, P. Millar, and X. Sun, "The geoscience laser altimeter system (glas) for the icesat mission," in *Conference on Lasers and Electro-Optics (CLEO 2000). Technical Digest. Postconference Edition. TOPS Vol.39 (IEEE Cat. No.00CH37088)*, pp. 602–603, 2000.

[24] R. Photonics, "Pulsed lasers," 2025. Accessed: 2025-03-10.

[25] KaranpreetVirk, "A review on self focusing in laser plasma interaction," *Materials Today: Proceedings*, vol. 37, pp. 2786–2791, 2021. International Conference on Newer Trends and Innovation in Mechanical Engineering: Materials Science.

[26] K. Wakker, *Fundamentals of Astrodynamics*. Jan 2015.

[27] J. Mason, J. Stupl, W. Marshall, and C. Levit, "Orbital debris-debris collision avoidance," *Advances in Space Research - ADV SPACE RES*, vol. 48, 03 2011.

[28] V. Morel, *Dynamique de la création d'un plasma d'aluminium induit par laser : Élaboration et validation d'un modèle collisionnel-radiatif.* Phd thesis, Université de Rouen, 2011. NNT : tel-04235881.

[29] A. Bogaerts, Z. Chen, R. Gijbels, and A. Vertes, "Laser ablation for analytical sampling: what can we learn from modeling?," *Spectrochimica Acta Part B: Atomic Spectroscopy*, vol. 58, pp. 1867–1893, 2003.

[30] D. Keil, S. Scharring, E. Klein, R.-A. Lorbeer, D. Schumacher, F. Seiz, K. Sharma, M. Zwilich, L. Schnörer, M. Roth, M. Ben-Larbi, C. Wiedemann, W. Riede, and T. Dekorsy, "Modification of space debris trajectories through lasers: Dependence of thermal and impulse coupling on material and surface properties," *Aerospace*, vol. 10, p. 947, 11 2023.

[31] B. Fontaine, "Modeling and simulation of electron distribution function in the VKI DRAGON facility," research master's thesis, von Karman Institute for Fluid Dynamics, 2024.

[32] C. Cai and I. Boyd, "Collisionless gas expanding into vacuum," *Journal of Spacecraft and Rockets - J SPACECRAFT ROCKET*, vol. 44, pp. 1326–1330, 11 2007.

[33] L. J. Radziemski, *Laser-Induced Plasmas and Applications*. New York: Marcel Dekker Inc., 1989.

[34] S. Li, J. Wang, X. Wang, Y. Cheng, and W.-C. Yan, "Mechanism analysis of space debris removal by nanosecond pulsed laser," *International Journal of Thermal Sciences*, vol. 192, p. 108451, 2023.

[35] E. S. D. Office, "Esa's annual space environment report," July 2024.